Applied Surface Science 581 (2022) 152103

Contents lists available at ScienceDirect

Applied Surface Science

journal homepage: www.elsevier.com/locate/apsusc

Full length article

Evolution of nanodiamond seeds during the chemical vapor deposition of diamond on silicon substrates in oxygen-rich plasmas

Alessandro Giussani *, Stoffel D. Janssens, David Vázquez-Cortés, Eliot Fried *

Mechanics and Materials Unit, Okinawa Institute of Science and Technology Graduate University (OIST), 1919-1 Tancha, Onna-son, Kunigami-gun, Okinawa, 904-0495, Japan

ARTICLE INFO

Keywords:
Detonation nanodiamond seeds
Nanocrystalline diamond
Microcrystalline diamond
Microwave plasma enhanced chemical vapor deposition
Nucleation
Coalescence

ABSTRACT

Methane, oxygen and hydrogen in relative concentrations of 1:0.5:98.5 were employed to deposit diamond films by microwave plasma enhanced chemical vapor deposition on Si(001) substrates seeded with detonation nanodiamonds of $5 \cdot 10^{10}\,\mathrm{cm}^{-2}$ density. The interaction between the nanodiamonds and the plasma was investigated as a function of the chamber pressure and the substrate temperature. At 40 Torr and 935 °C, 90% of the seeds were etched, and growth induction occurred with an impractically long time of 23.5 h. Varying the substrate temperature between 827 °C and 935 °C did not lead to faster growth induction. Reducing the chamber pressure to 30 Torr instead resulted in continuous films with induction time as short as 12 min. The induction time and the growth rate exhibited an Arrhenius dependence in the temperature range 769–884 °C with apparent activation energies of 3.7 eV/atom and 0.3 eV/atom, respectively. When at 30 Torr the concentration of the oxygen additive was raised to 1 vol%, the seeds were completely dissolved and no film deposition took place. However, film growth was possible with an oxygen admixture as high as 1.5 vol% on a diamond precursor layer of approximately 55 nm thickness, which was nucleated in an oxygen-free plasma.

1. Introduction

Nanocrystalline diamond (NCD) films and coatings formed by chemical vapor deposition (CVD) have applications in machining [1–4], sliding and rotating bearings [5,6], field-induced electron emission [7–12], optoelectronics [13], quantum computing [14–16], dentistry [17,18], biomedicine and biotechnology [10,19–22], and sensing via micro- and nanoelectromechanical systems [23–25]. The quality of NCD material is strongly dependent on both the nucleation process and the growth conditions [26,27]. Nucleation is challenging because NCD films and coatings are deposited on foreign substrates that are physically and chemically dissimilar to diamond. A representative case is provided by silicon, one of the most widely employed substrates for NCD growth. The ≈34% smaller lattice parameter and circa fourfold higher surface energy of diamond relative to silicon, the small sticking coefficient of the gas precursors, the low adatoms' mobility and the competing formation of non-diamond carbon concur to yield on unprocessed silicon substrates a nucleation density of only 10^4–$10^5\,\mathrm{cm}^{-2}$, which is insufficient for inducing film growth [28–30]. Pretreatment of the initial surface is hence required to aid nucleation, e.g., *ex situ* immersion of the substrate in an aqueous or alcohol suspension of nanodiamond particles in ultrasonic bath or *in situ* exertion of a negative bias between the substrate electrode and a surrounding grounded electrode during the preliminary CVD steps [28,29,31]. A high nucleation density hinders the formation of voids at the substrate–film interface improving film adhesion, reduces undesired non-diamond carbon inclusions and leads to smoother deposits [30]. Importantly, a Young's modulus approaching the single crystal value of 1200 GPa was achieved for NCD films by increasing the density of the seeds from approximately 10^{10} to $10^{12}\,\mathrm{cm}^{-2}$ [32]. The growth parameters afford control over the grain size and the crystal orientation [33,34] and also of the purity of the material and other physical properties [35]. For instance, NCD films with Young's moduli as high as 1100 GPa were deposited by microwave chemical vapor deposition (MWCVD) using methane concentrations less than or equal to 1 vol% in H_2. Increasing the methane concentration and decreasing the plasma power density resulted in smaller crystallite size, larger content of sp^2 and hydrogen in the grain boundaries in conjunction with a degradation of the mechanical characteristics of the films [36].

Adding a small amount of oxygen to the hydrocarbon and hydrogen gas mixture is one way of improving NCD film quality [28,37]. Oxygen indeed hinders the formation of non-diamond carbon [38–41] and the incorporation of foreign atoms such as hydrogen [42], boron [43–45] and silicon [39,46,47]. Employing an oxygen additive can lead to further functionalities and benefits. For instance, oxygen supplied

* Corresponding authors.
E-mail addresses: giussani.alessandro@gmail.com (A. Giussani), eliot.fried@oist.jp (E. Fried).

https://doi.org/10.1016/j.apsusc.2021.152103
Received 27 October 2021; Received in revised form 23 November 2021; Accepted 29 November 2021
Available online 29 December 2021

as water vapor during hot filament CVD (HFCVD) was very recently shown to permit the modulation of the wettability of NCD films *in situ* in a cost-effective manner, which has tremendous potential for biotechnology [48]. Moreover, oxygen, typically in the form of CO_2, is used as a means to achieve low growth temperatures in the plasma-enhanced CVD of diamond films [49,50] and diamond nanostructures [51], which is critical to applications requiring temperature-sensitive substrates such as plastic. Numerous studies have been carried out to elucidate the impact of an oxygen admixture on the overall film attributes. However, to the best of our knowledge, the initial stages of growth in the presence of an oxygen additive have not been explored yet. The stability of the detonation nanodiamond seeds is especially crucial during the growth of diamond films on a foreign substrate and is therefore investigated in this work. Specifically, (001)-oriented silicon substrates were seeded with detonation nanodiamonds and were subsequently exposed to a plasma of methane and oxygen in hydrogen. The interaction of the nanodiamonds with the oxygen-rich plasma was studied as a function of the chamber pressure and the sample temperature by means of *in situ* laser interferometry and *ex situ* secondary electron microscopy (SEM). For deposition conditions that permitted film growth, the diamond films were characterized using *ex situ* SEM, white light reflectometry, atomic force microscopy (AFM), Raman spectroscopy and X-ray diffraction (XRD). It was found that the growth window is primarily determined by the interplay between the chamber pressure and the oxygen admixture concentration, and can be expanded towards high oxygen concentrations by introducing a preliminary deposition step without an oxygen additive. It was also observed that the initial stages of growth are governed by a surface reaction with an apparent activation energy that is approximately one order of magnitude larger than the apparent activation energy typically reported for diamond film growth.

2. Materials and methods

2.1. Seeding and deposition

2 cm × 2 cm substrates were cleaved out of Czochralski, single-side polished silicon wafers with 100 mm diameter, 525 ± 25 µm thickness, (100) orientation, n-doping (phosphorous), resistivity 1–10 Ω · cm, supplied by *Electronics and Materials Corporation Limited*. The cleaved silicon substrates underwent in sequence 5 min ultrasonic bath in acetone, 5 min ultrasonic bath in isopropanol, rinse in deionized (DI) water, 15 min cleaning in a 5:1:1 solution of DI H_2O:NH_4OH:H_2O_2 at 70°C (the *SC-1* step of the *RCA* cleaning process, where *SC* and *RCA* stand for *Standard Clean* and *Radio Corporation of America*, respectively [52]), rinse in DI water and drying under blown nitrogen. 0.1 g of a powder of detonation nanodiamonds with primary particle size 3.9 ± 0.7 nm and density $1 \cdot 10^{19}$ g^{-1}, purchased from *NanoCarbon Research Institute Co., Ltd.*, were dispersed in 0.2 l of DI water and ultrasonicated as described in [53]. The resulting suspension appeared turbid and was centrifuged at 7500 rpm and 20 °C for 1 h to sediment particles. Seeding of the silicon substrates was carried out as follows. First, each cleaned silicon piece was treated in a *Yamato Plasma Reactor PR200* in a plasma of air (flow 100 sccm, pressure 10 Torr, plasma input power 170 W, duration 60 s), aiming at enhancing the wettability of the substrate. Next, the silicon piece was transferred onto the stage of a spin coater and 180 µl of the suspension were drop-cast on its surface. Immediately after the casting, the substrate was spun for 25 s at 4000 rpm while flushing with DI water for the first 10 s to minimize aggregation of the nanodiamonds. It is stressed that the time elapsed between the plasma treatment and the seeding was consistently limited to a few seconds to prevent the contamination of the substrate surface with adventitious hydrocarbons, which was recently proven to affect the contact angle of the colloidal suspension on the surface and the seed density [54]. This protocol reproducibly led to a seed density on the order of $5 \cdot 10^{10}$ cm^{-2} so that circa 20% of the surface was covered, as verified by SEM inspection on several seeded substrates (Supplementary Figure 1(a)). A similar seeding procedure yielded NCD films of high quality on glass substrates as well [53,55]. The seeded template was loaded onto a hollow molybdenum block, lying on the water-cooled copper stage of a commercial *SDS6500X* MPCVD system manufactured by *Cornes Technologies Ltd.* The chamber was pumped down to a base pressure of 60 mTorr by means of a *Kashiyama SDE90X* dry pump. The cavity between the hollow molybdenum holder and the copper stage, the so called *plenum*, was differentially pumped via an orifice in the center of the copper stage to a pressure between the chamber operative pressure and the base pressure. Hereafter, P_{ch} and P_{pl} will denote the chamber pressure and the plenum pressure, respectively. Two chamber pressures, $P_{ch} = 30$ Torr and 40 Torr, were investigated. These chamber pressures were chosen because they allow for an ample space of deposition parameters in our reactor when a gas feed of methane and hydrogen is employed. Moreover, they were reported by other groups to yield high quality NCD films for plasma forward powers and gas mixtures similar to the ones used in our work [56]. Hydrogen, methane and oxygen with purity >99.9999% were pre-mixed in the desired ratios and introduced in the chamber as reactant gas. The methane concentration [CH_4] was fixed to 1 vol%, whereas the oxygen concentration [O_2] was varied between 0 and 1.5 vol%. The total gas flow $\Phi_{tot} = \Phi(CH_4) + \Phi(O_2) + \Phi(H_2)$ was set to 500 standard cubic centimeter per minute (sccm). The plasma was activated by a magnetron generating 2.45 GHz electromagnetic waves with a maximum forward power of 6000 W. The plasma forward power P_{fw} was 4000 W in all the experiments. The sample was heated up by the microwaves and via convection from the plasma gas [57], and its temperature was tuned by controlling P_{pl} as shown in Figs. 2(e) and 3(a), exploiting the dependence of the thermal conductance of the plenum cavity on the pressure. A lower limit to the range of accessible temperatures existed because of the condition $P_{pl} \leq P_{ch}$ and, without a sample heater, both the reduction of P_{ch} and the introduction of oxygen caused an unsought decrease of the sample temperature at a given P_{pl}. At the start of the run, P_{fw}, P_{ch}, P_{pl} and the gas flows were ramped up in steps using an automatic routine. The deposition time t_{dep} was 6 h unless differently specified and was counted starting from when steady growth conditions, namely, the stable growth temperature, were attained. After the growth time had elapsed, the methane and oxygen flows were instantaneously cut, and cooling down was carried out in a plasma of pure hydrogen while the chamber pressure and the plasma power were gradually reduced until plasma shutdown, again employing a software recipe. Deposition parameters for $P_{ch} = 40$ Torr and 30 Torr are listed in Tables 1 and 2, respectively.

It is noted that some of the samples discussed hereafter may be classified as microcrystalline diamond (MCD) films, depending on which naming convention is employed [26,29,37,58]. For this reason, in the following the samples are generically referred to as diamond films. Since for the employed deposition conditions NCD films evolve into MCD films as the film thickness increases, the conclusions of our work regarding the initial stages of growth are applicable to both NCD and MCD films.

2.2. Characterization

Samples were characterized by multiple techniques. Growth progress was monitored by means of a homemade *in situ* interferometer employing a 532 nm laser source and a narrow pass-band filter in front of a silicon photodiode. The angle between the impinging laser beam and the sample surface normal was fixed to 25°. The diamond film thickness corresponding to a full period oscillation of the interferometer signal was estimated to be 113 nm using the formula that appears in the work of Saada et al. [59] and assuming a refractive index of 2.4 for diamond. The temperature T of the specimen was monitored *in situ* by means of an infrared thermometer with 0.970–1.625 µm spectral bandwidth from *Japan Sensor Corporation*. The sample emissivity was set to 0.65 [60,61]. From Tables 1 and 2, it is evident that the

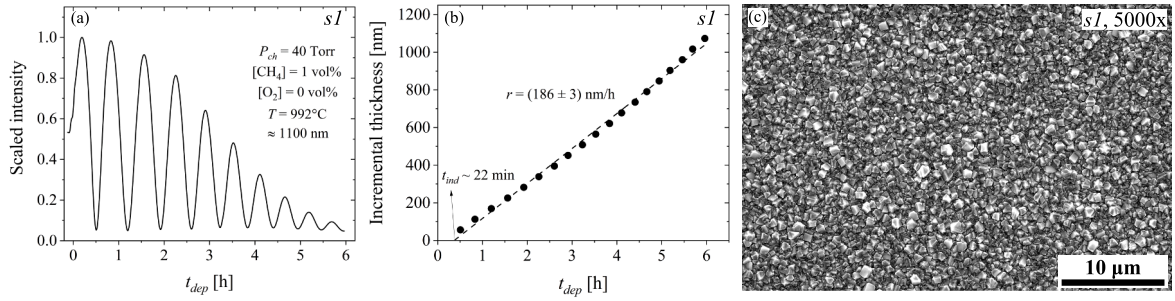

Fig. 1. MWCVD at P_{ch} = 40 Torr from a gas feed of 1 vol% CH_4 in H_2 without oxygen additive (sample *s1* of Table 1). (a) *In situ* interferometer curve. (b) Plot of the incremental film thickness as a function of t_{dep}. The thickness increment is 56.5 nm, which is the thickness estimated to grow in between any two consecutive extrema of the interferometer curve after the first minimum. The dashed line represents the least squares regression line of the data points. Its intercept with the *x*-axis and its slope provide the induction time t_{dep} (22 min) and the film deposition rate (186 nm/h), respectively. (c) SEM plan-view with magnification 5000× of the final surface.

uncertainty of the temperature was larger for recipes yielding a film. This is because, during film growth, the radiation emitted from the specimen was modulated by optical interference at the substrate–film interface and at the film surface, which generated apparent temperature oscillations in the pyrometer signal [62]. The sample surface was characterized *ex situ* using a *FEI Quanta 250 FEG* SEM and a *Bruker Dimension ICON3* AFM equipped with silicon probes with 7 nm (14 µm) tip radius (length), 300 KHz resonant frequency and 26 N/m spring constant, imaging in tapping mode. The density and the surface coverage of the nanodiamond seeds and of the particles detected on the non-coalesced specimens were estimated by digitally processing SEM micrographs with a self-made *Python* program. The total layer thickness was measured *ex situ* with an *Optical NanoGauge C13027-12* from *Hamamatsu Photonics K. K.*, mounting a halogen light source. The fitting was performed assuming a simple layer stack model consisting of a diamond film on a silicon substrate. The accuracy of the thickness estimate was verified by means of SEM cross-sections (Supplementary Figures 1(b–c)).

A structural and chemical characterization via XRD and Raman spectroscopy of diamond films deposited with an oxygen admixture is presented in Section Supplementary 3 of the Supplementary Material.

3. Results and discussion

3.1. Reference growth, induction time, and growth rate

When film growth begins, the interferometer signal is expected to start oscillating as the beams reflected by the gas–film interface and the film–silicon interface alternately undergo destructive and constructive interference. This effect is exemplified in Fig. 1(a), which shows the curve obtained for the MWCVD of a diamond film at P_{ch} = 40 Torr from a gas feed of 1 vol% CH_4 in H_2 without oxygen additive (specimen *s1* of Table 1). For approximately 5 min whilst the plasma was fired and its forward power was gradually ramped up, the intensity of the signal steeply rose owing to the increase of the reflectance of the silicon substrate with the temperature [59]. A secondary contribution to the increment of the signal was provided by stray light stemming from the plasma ball and the heating of the specimen, which progressively intensified during the plasma ramp-up and entered the photodetector, thereby compounding effects due to the laser light reflected from the sample surface. A delay in the onset of the oscillations is a measure of the duration of the so called growth incubation or induction [29,63], a preliminary stage to the formation of diamond during which carbon supersaturation of the substrate surface occurs via chemical interactions with activated gas species. The incubation produces an intermediate layer containing non-diamond carbon, whose nature, thickness, phase and growth kinetics strongly depend on the substrate material and the deposition parameters [64]. In the case of silicon substrates, the interfacial layer is typically reported to be a silicon carbide with a thickness in the range of a few nm [65–77]. Once the silicon carbide has reached a critical thickness, it functions as a barrier against further inter-diffusion between carbon and silicon [78], and carbon excess becomes available on the surface to generate diamond nuclei in the case of an untreated substrate or to initiate seed growth in the case of a pretreated template. It is noted that, after the incubation, the appearance of thickness fringes in the interferometer curve may be further hampered by a slow lateral growth of the nuclei/seeds on the heterogeneous substrate surface, as illustrated in Section 3.2. Disentangling the two phenomena of incubation and coalescence into a closed film is not straightforward and falls outside the scope of this work.

Herein, the induction time t_{ind} is defined as the intercept with the *x*-axis of the linear regression of the incremental film thickness as a function of the deposition time t_{dep}, and represents the duration of the stage(s) preceding the growth of a closed diamond film. The method for extracting a value for t_{ind} is indicated in Fig. 1(b), which shows that t_{ind} = 22 min for specimen *s1*. The slope of the linear regression of Fig. 1(b) yields the average growth rate *r* over the period between the first local minimum and the last extremum in the interferometer curve (186 nm/h). The SEM image of Fig. 1(c) reveals a continuous pinhole-free diamond film.

3.2. Oxygen addition

A seeded silicon substrate was exposed to the reactor parameters of sample *s1*, except that an oxygen admixture of 0.5 vol% was added to the gas feed (sample *s2* of Table 1). The introduction of oxygen resulted in a markedly different growth scenario with respect to the oxygen-less deposition of sample *s1*. Fig. 2(a) illustrates the interferometer curve recorded *in situ*. It is immediately noticeable that the profile spans 30 h versus the 6 h of Fig. 1(a). For the reason outlined in the description of Fig. 1(a), the interferometer signal steeply increased during the ramp-up of the plasma. Here, however, the subsequent decrease of the intensity did not quickly lead to a local minimum and to growth oscillations. The signal rather stabilized, remaining nearly constant for 18 h until a marked drop to a local minimum occurred. Afterwards, the interferometer curve displayed thickness fringes, attesting to the growth of a diamond film at a rate of 40 nm/h, which amounts to circa 20% of the growth rate of sample *s1*. To gain insight into the evolution of the surface over the deposition of 30 h, SEM plan-views were taken of the final surface and at different stages into the process by preparing new specimens with intermediate deposition times of 6 h and 18 h (*s3* and *s4* of Table 1, respectively). Fig. 2(b) shows that after 6 h the spin-coated seeds did not develop into a film, unlike the oxygen-less deposition of sample *s1*, which yielded a compact film of 1100 nm within the same deposition time. Instead, the surface features sparse particles with a density of $6 \cdot 10^9$ cm^{-2} and a surface coverage of 3% along with pits as wide as 300 nm, revealing that 90% of the spin-coated seeds and the silicon surface were etched by the plasma. Compared to the state of

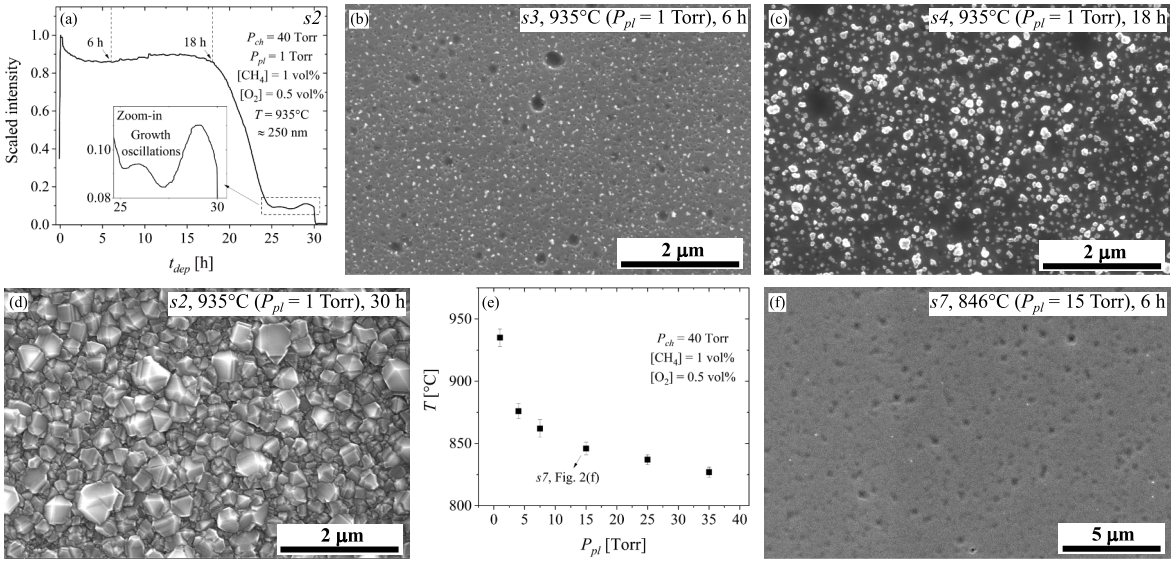

Fig. 2. MWCVD process at P_{ch} = 40 Torr from a gas feed of 1 vol% CH_4 and 0.5 vol% O_2 in H_2. (a) Interferometer signal recorded *in situ* during the 30 h long deposition of sample *s2* of Table 1. The vertical dashed lines mark the deposition times of 6 h and 18 h, which were employed to grow samples *s3* and *s4* of Table 1, respectively. The zoomed-in inset shows signal oscillations attesting to the growth of a diamond film in the interval t_{dep} ≈25–30 h. (b) SEM image of the surface after 6 h of deposition (sample *s3*). (c) SEM image of the surface after 18 h of deposition (sample *s4*). (d) SEM image of the surface after 30 h of deposition (sample *s2*), proving that a closed diamond film formed after an extremely sluggish induction. The total film thickness was measured to be approximately 250 nm by *ex situ* white light reflectometry. (e) Dependence of the average sample temperature *T* on the plenum pressure P_{pl} for samples *s3*, *s5-9* of Table 1, deposited for 6 h. (f) SEM image of the surface after 6 h of deposition with P_{pl} = 15 Torr, showing that lowering the substrate temperature is not conducive to thin film growth within the 6 h time frame, but rather results in a harsher etch of the seeds (sample *s7* of Table 1).

the surface 6 h into the deposition, after 18 h the density of diamond crystallites remained unchanged but the average particle size increased, resulting in a circa tenfold higher surface coverage (Fig. 2(c)). Fig. 2(d) demonstrates that after 30 h a closed faceted diamond film formed. Interpreting the interferometer data in light of the SEM results, the first, gentler decay of the signal of Fig. 2(a) is attributed to the roughening of the sample surface, which is a consequence of the etch of the silicon substrate and the seeds evidenced by Fig. 2(b). Silicon is known to be attacked by atomic hydrogen [79,80] and was reported to etch off during diamond HFCVD experiments employing diluted feeds of CH_4 in H_2 [75]. The seeds likely etched off because of their high defectivity. Indeed, detonation nanodiamonds are affected by both structural and compositional faults intrinsic to the detonation process. Twinning is the most common crystallographic flaw [81,82]. Nitrogen atoms from the explosives tend to remain embedded with tetrahedral coordination in the kernel of the nanodiamonds, and the concentration of nitrogen impurities increases with the size of the nanoparticle. Furthermore, nanodiamonds are surrounded by a graphitic shell [81, 83–88]. We allege that the majority of the spin-coated nanodiamonds were highly defective and were therefore etched by the hydrogen and oxygen radicals present in the plasma, and that only the more perfect crystallites were enlarged by effectively incorporating carbon atoms from the precursor, triggering film coalescence and growth. On this regard, it is noted that, in a comprehensive investigation of the MWCVD stability of detonation nanodiamonds on silicon by Arnault et al., the initial seed density was reduced by up to 3.5 times following a H_2 plasma pretreatment aimed at removing sp^2 carbon and enhancing the adhesion of the nanoparticles to the substrate [76]. In our experiments, involving an oxygen additive and a higher plasma power, structural and compositional imperfections may be more prone to etch than in a pure H_2 environment, leading to a higher loss of the seeds (a factor of ≈10, from $\approx 5 \cdot 10^{10}$ cm^{-2} to $\approx 6 \cdot 10^{9}$ cm^{-2}).

The second, more pronounced drop of intensity in Fig. 2(a) is assigned to the induction taking place with a time constant of 23.5 h, which is circa 65 times longer than for the growth of sample *s1* carried out without an oxygen admixture under otherwise identical conditions. The sluggish onset of thickness oscillations in the interferometer curve is likely linked to the heavy etch of the seeds discussed above. According to the theory of nucleation of thin films, nuclei already existing on the surface, such as the seeds, are predicted to enlarge by the direct impingement of species from the vapor phase and the capture of adatoms at a rate which is proportional to the nuclei circumference and the adatoms' diffusion coefficient [89]. Diamond clusters smaller than a critical size are either etched into the gas phase by hydrogen radicals or aggregate to reach the critical size and form stable nuclei [71, 73,90,91]. Since heterogeneous nucleation is hindered, it is to be expected that coalescence into a thin film occurs on a longer time scale the more seeds are etched by the plasma. The presence of activated oxygen species may also slow down the carbon supersaturation of the outermost layers of the substrate and the adatoms' diffusivity.

Since both the sticking coefficient of the vapor species and the diffusion coefficient of the adatoms on the surface depend on the substrate temperature [89], and the literature contemplates the achievement of optimized diamond film nucleation by tuning the substrate temperature [65,92,93], it was decided to explore also the impact of the substrate temperature on the induction. A set of specimens were grown for 6 h at different P_{pl} set-points (samples *s5-9* in Table 1, adding to the already existing sample *s3* for P_{pl} = 1 Torr). The data points of Fig. 2(e) show that the growth temperature diminished with P_{pl} steeply between 1 and 4 Torr and weakly beyond 4 Torr, spanning the range 827–935 °C. None of the samples of the series evolved into a diamond film, as the absence of thickness fringes in the corresponding interferometer curves indicated *in situ* (not shown). In fact, reducing the temperature within the range accessible via P_{pl} control turned out to be detrimental. It resulted in a more aggressive etch of the substrate and of the seeds until their complete disappearance. This is representatively illustrated by the SEM photograph of the surface of sample *s7* deposited at P_{pl} = 15 Torr (Fig. 2(f)).

3.3. Oxygen addition and lower pressure

The effect of reducing the chamber pressure from 40 to 30 Torr on the process with 1 vol% CH_4 and 0.5 vol% O_2 in H_2 was studied. The supposition is that a lower chamber pressure may exert a milder

Table 1
MWCVD parameters of the samples processed at a chamber pressure P_{ch} = 40 Torr. The plasma forward power P_{fw}, the methane concentration [CH_4] and the total gas flow $\Phi_{tot} = \Phi(CH_4) + \Phi(O_2) + \Phi(H_2)$ were set to 4000 W, 1 vol% and 500 sccm, respectively. δ (σ) represents the surface density (coverage) of either the spin-coated seeds pre-CVD deposition or the residual particles detected on the surface after the CVD process in case thin film growth did not take place.

Sample ID	P_{ch} [Torr]	P_{pl} [Torr]	T [°C]	[O_2] [vol%]	t_{dep} [min]	Total thickness [nm]	Outcome
s1	40	1	992 ± 14	0	360	1100	Continuous film (Fig. 1(c))
s2 (s3, s4†)*	40	1	935 ± 7	0.5	1800	250	Continuous film (Fig. 2(d))
					*360	–	Residual particles ($\delta \approx 6 \cdot 10^9$ cm^{-2}; $\sigma \approx 3\%$); sub-µm-size pits (Fig. 2(b))
					†1080	–	Growing particles ($\delta \approx 5 \cdot 10^9$ cm^{-2}; $\sigma \approx 27\%$); sub-µm-size pits (Fig. 2(c))
s5	40	4	876 ± 6	0.5	360	–	Fewer particles ($\delta \approx 5 \cdot 10^7$ cm^{-2}) and higher density of sub-µm-sized pits than in sample *s3* (not shown)
s6	40	7.5	862 ± 7	0.5	360	–	No residual particles; sub-µm-sized pits (not shown)
s7	40	15	846 ± 5	0.5	360	–	No residual particles; sub-µm-sized pits (Fig. 2(f))
s8	40	25	834 ± 4	0.5	360	–	No residual particles; sub-µm-sized pits (not shown)
s9	40	35	827 ± 4	0.5	360	–	No residual particles; sub-µm-sized pits (not shown)

Table 2
MWCVD parameters of the samples processed at a chamber pressure P_{ch} = 30 Torr. For all the specimens, the plasma forward power P_{fw}, the methane concentration [CH_4] and the total gas flow $\Phi_{tot} = \Phi(CH_4) + \Phi(O_2) + \Phi(H_2)$ were 4000 W, 1 vol% and 500 sccm, respectively. In samples *s18* and *s19*, a diamond film was grown without any oxygen additive up to the first local minimum of the interferometer curve (precursor layer). Afterwards, an oxygen admixture of 1 vol% (1.5 vol%) was added to the gas feed in sample *s18* (*s19*) and the deposition was continued for 6 h. For these samples, the deposition parameters in the table except the total thickness refer to the second and main deposition step. The total film thickness was assessed *ex situ* by white light reflectometry. The thickness of *s11* was estimated by measuring the depth of the pinholes reaching the silicon substrate in AFM images such as the one of Fig. 4(b).

Sample ID	P_{ch} [Torr]	P_{pl} [Torr]	T [°C]	[O_2] [vol%]	t_{dep} [min]	Total thickness [nm]	Outcome
s10 (s11‡)	30	1	884 ± 11	0.5	360	860	Continuous film (Fig. 3(b))
					‡30	50	Continuous film (Fig. 4(b))
s12	30	4	841 ± 11	0.5	360	765	Continuous film (Fig. 3(c))
s13	30	8	809 ± 10	0.5	360	620	Continuous film (Fig. 3(d))
s14	30	16	789 ± 11	0.5	360	530	Continuous film (Fig. 3(e))
s15 (s16¶)	30	25	769 ± 12	0.5	360	420	Continuous film (Fig. 3(f))
					¶30	–	Non-coalesced seeds (Fig. 4(c))
s17	30	1	798 ± 7	1	360	–	No residual particles; sub-µm-size pits (Fig. 5(b))
s18	30	1	830 ± 16	1	360	410	Continuous film (Fig. 5(c))
s19	30	1	836 ± 6	1.5	360	190	Continuous film (Fig. 5(d))

attack on the nanodiamond seeds and on the silicon substrate in the early MWCVD stages. Such a rationale was put forward by Buchkremer-Hermanns et al. to explain why the nucleation density on treated Si_3N_4 templates considerably increased with decreasing P_{ch} in a MWCVD apparatus using CH_4 and H_2 gas mixtures [94]. Analogously, Kim et al. found that, in the HFCVD of diamond from a CH_4 and H_2 feed on unscratched Si(100) wafers, the nucleation density could be enhanced by more than an order of magnitude by reducing the chamber pressure from 50 to 5 Torr [95]. A few years after the work of Kim et al., Lee et al. established the use of even lower chamber pressures in the 0.1–1 Torr range to obtain unprecedented nucleation densities of 10^{10}–10^{11} cm^{-2} on untreated silicon substrates employing 2 vol% CH_4 in H_2 in HFCVD. They attributed the enhanced nucleation at low pressure to an augmented mean free path that resulted in a larger concentration of nucleating species on the silicon surface [96].

A new series of specimens were therefore created at P_{ch} = 30 Torr for increasing P_{pl} set-points (samples *s10, s12–15* in Table 2), similar to the temperature-dependent study at P_{ch} = 40 Torr outlined in Section 3.2. Fig. 3(a) shows that the temperature interval that could be covered at P_{ch} = 30 Torr was 769–884 °C, which is shifted downwards by approximately 50 °C with respect to P_{ch} = 40 Torr. In stark contrast to the surface of the specimens deposited for 6 h with a 0.5 vol% O_2 additive at P_{ch} = 40 Torr (Figs. 2(b, f)), the SEM images of Figs. 3(b–f) show that after 6 h at P_{ch} = 30 Torr a compact diamond film was obtained at any temperature within the explored range. Furthermore, the size of the crystallites was observed to increase as the temperature was lowered despite a decrease of the film thickness (Fig. 4(f)). To unveil how the growth evolved during the 6 h of deposition time, an interferometer curve was taken *in situ* for each specimen. All the curves exhibited thickness fringes at a certain point into the deposition, indicating that the growth of a continuous film was taking place. For the sake of clarity, Fig. 4(a) presents only three representative curves for the highest, middle and lowest deposition temperatures. Two preliminary qualitative observations can be made by examining the graph.

Firstly, the time to achieve the first minimum of the interferometer curve clearly increased with P_{pl}, implying that thin film growth started with a larger delay when the substrate temperature was reduced. The trend can be visually appreciated by looking at the AFM images of Figs. 4(b, c), which portray the morphology of the surface of two additional specimens deposited at the highest and the lowest temperature, respectively, for only 30 min. At this deposition time, the black curve of Fig. 4(a), recorded at 884 °C (P_{pl} = 1 Torr), was approaching the first local minimum. Correspondingly, Fig. 4(b) shows the existence of a diamond film. In contrast, the green curve of Fig. 4(a), logged at 769 °C (P_{pl} = 25 Torr), was still in the initial plateau after 30 min and accordingly Fig. 4(c) reveals non-coalesced seeds, attesting that the MWCVD process was in an embryonal phase of the induction when the run ended. The induction time was calculated for all the specimens of the series, as outlined in Section 3.1 for sample *s1*. Its dependence on the substrate temperature is illustrated in Fig. 4(d). From dimensional analysis it is inferred that

$$t_{ind} \propto 1/r_{ind}, \tag{1}$$

where r_{ind} is an induction rate that can be described by an Arrhenius relation of the type

$$r_{ind} \propto \exp(-E_{A,ind}/K_B T), \tag{2}$$

where $E_{A,ind}$, K_B, and T are the apparent activation energy of the induction process, the Boltzmann constant, and the absolute temperature on the Kelvin scale, respectively. Combining (1) and (2), the induction time can be written as

$$t_{ind} = t_{ind,0} \exp(E_{A,ind}/K_B T), \tag{3}$$

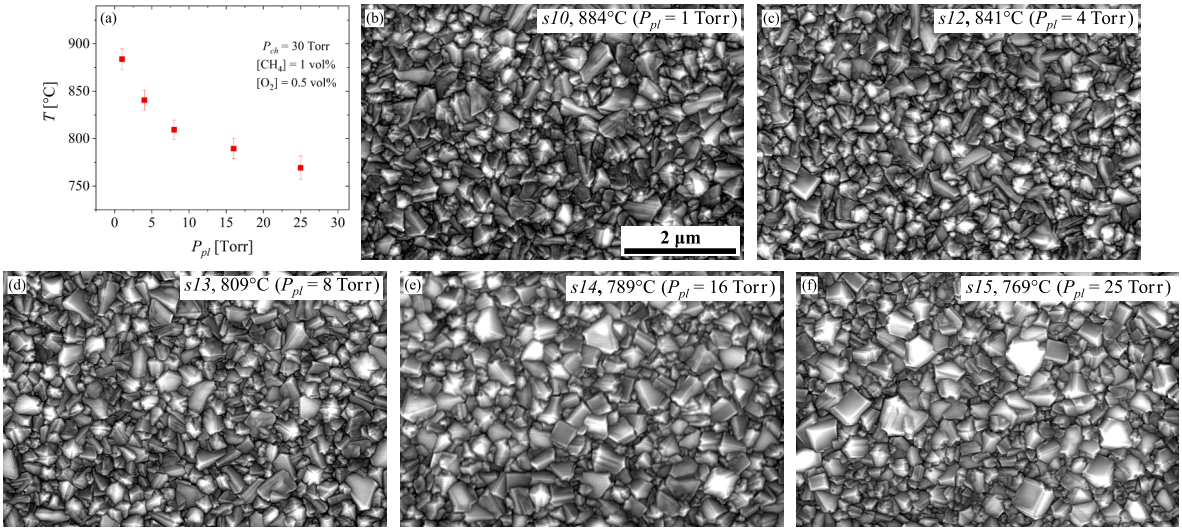

Fig. 3. MWCVD process at P_{ch} = 30 Torr from a gas feed of 1 vol% CH_4 and 0.5 vol% O_2 in H_2. (a) Dependence of the average substrate temperature on the plenum pressure P_{pl}. Temperature data and other deposition parameters of the here displayed specimens are summarized in Table 2. 30000× magnified SEM images of the final surface of sample (b) *s10* (P_{pl} = 1 Torr → T = 884 °C), (c) *s12* (P_{pl} = 4 Torr → T = 841 °C), (d) *s13* (P_{pl} = 8 Torr → T = 809 °C), (e) *s14* (P_{pl} = 16 Torr → T = 789 °C) and (f) *s15* (P_{pl} = 25 *Torr* → T = 769 °C).

where $t_{ind,0}$ is the asymptotic induction time for $T \rightarrow \infty$. The data points of Fig. 4(d) can be fitted to (3), thereby implying that the time-limiting factor in the induction process is a temperature-dependent surface reaction with $E_{A,ind}$ = 3.7 ± 0.4 eV/atom (86 ± 9 kcal/mol). To the best of our knowledge, this is the first time that a value of the activation energy of the growth induction of a diamond thin film on a foreign substrate in the presence of an oxygen additive has been provided.

Secondly, Fig. 4(a) shows that, beyond the first local minimum, the period of the fringes decreased with the substrate temperature. Since a full oscillation corresponds to the deposition of approximately 113 nm of diamond material, this means that the deposition rate increased with the temperature. The dependence is depicted in the Arrhenius plot of Fig. 4(e) and was found to be represented by the Arrhenius relation

$$r = r_0 \exp(-E_{A,g}/K_B T), \tag{4}$$

where r, r_0, and $E_{A,g}$ are the deposition rate, the asymptotic deposition rate, namely, the deposition rate for $T \rightarrow \infty$, and the apparent activation energy of the growth process, respectively. The least squares regression of the natural logarithm of the deposition rate data points as a function of the reciprocal absolute temperature yielded an apparent activation energy $E_{A,g}$ of 0.3 ± 0.05 eV/atom (7 ± 1 kcal/mol), which is approximately an order of magnitude smaller than the activation energy $E_{A,ind}$ of the induction process (Fig. 4(e)). The derived value of $E_{A,g}$ is within the range of values reported in the literature, namely ≈0.07–1.30 eV/atom (1.7–30 kcal/mol), which strongly depend on the employed deposition method, gas mixture and reactor geometry [49, 97–99]. However, there are also accounts of the growth rate increasing monotonically with the substrate temperature without obeying an Arrhenius law [100]. As a last comment on Figs. 4(d–e), it is conjectured that controlling the temperature of the specimen independently from the plasma variables by means of a dedicated heater could help reduce data scattering, as pointed out by Kondoh et al. [101]. Since the induction became longer and the deposition rate slowed down as the substrate temperature was diminished by raising P_{pl}, within the fixed 6 h of deposition the total thickness of the diamond film decreased. This is evident from Fig. 4(a), which visibly shows that the number of thickness fringes is proportional to the substrate temperature, and was quantitatively verified by measuring the total film thickness independently from the interferometer spectra using *ex situ* the *Optical NanoGauge*. Fig. 4(f) illustrates the dependence. Notably, at the low end of the growth temperature interval, the 20% reduction in film thickness passing from 789 °C to 769 °C is mostly ascribable to the 155% longer induction (Fig. 4(d)). Thickness estimates obtained by *in situ* interferometry as detailed in the caption of Fig. 4 and by SEM cross-sections on selected specimens (Supplementary Figures 1(b–c)) were added to the graph and exhibit a good agreement with the thickness values assessed by *ex situ* reflectometry.

A structural, morphological and chemical characterization of the diamond films is presented in Section Supplementary 3 of the Supplementary Material.

3.4. Two-stage growth: enabling large oxygen concentrations

When larger oxygen concentrations were employed at P_{ch} = 30 Torr, e.g., [O_2] was raised from 0.5 to 1 vol% (sample *s17* of Table 2), the interferometer curve did not exhibit thickness oscillations (black curve in Fig. 5(a)), indicating an absence of film growth. In line with the *in situ* data, the *ex situ* SEM image of the surface reveals that the seeds completely etched off in spite of the low chamber pressure P_{ch} = 30 Torr (Fig. 5(b)). This suggests that, for a given set of plasma power, chamber pressure, total gas flow and methane concentration, there is an upper concentration of the oxygen admixture [O_2] in the gas feed, above which the seeds cannot survive the plasma. However, the threshold parameters for the survival of the seeds did not coincide with the threshold conditions for thin film growth. When the seeds on a clean silicon substrate were first allowed to coalesce in the absence of an oxygen admixture ([CH_4] = 1 vol%, [O_2] = 0 vol%, P_{ch} = 30 Torr) and then the growth conditions were switched to the ones of sample *s17* ([CH_4] = 1 vol%, [O_2] = 1 vol%, P_{ch} = 30 Torr), the film continued growing as demonstrated by the thickness oscillations in the red interferometer curve of Fig. 5(a) (sample *s18* in Table 2). The SEM image of the final surface in Fig. 5(c) shows the presence of a continuous diamond film. Noteworthily, after the deposition of a diamond precursor layer in an oxygen-less plasma, growth took place even in the presence of a 1.5 vol% [O_2] admixture, as proven by the thickness fringes in the green interferometer curve of sample *s19* in Fig. 5(a). The post-deposition SEM micrograph of sample *s19* is presented in Fig. 5(d) and confirms the growth of a compact diamond film. Hence, based on the results illustrated in Fig. 5 and the previous finding, that the diamond net growth rate of specimen *s2* turned out to be 40 nm/h albeit an induction of 23.5 h, it is concluded that in an oxygenated plasma nanoseeds behave differently to the crystallites of a compact diamond film. A similar observation was made about the

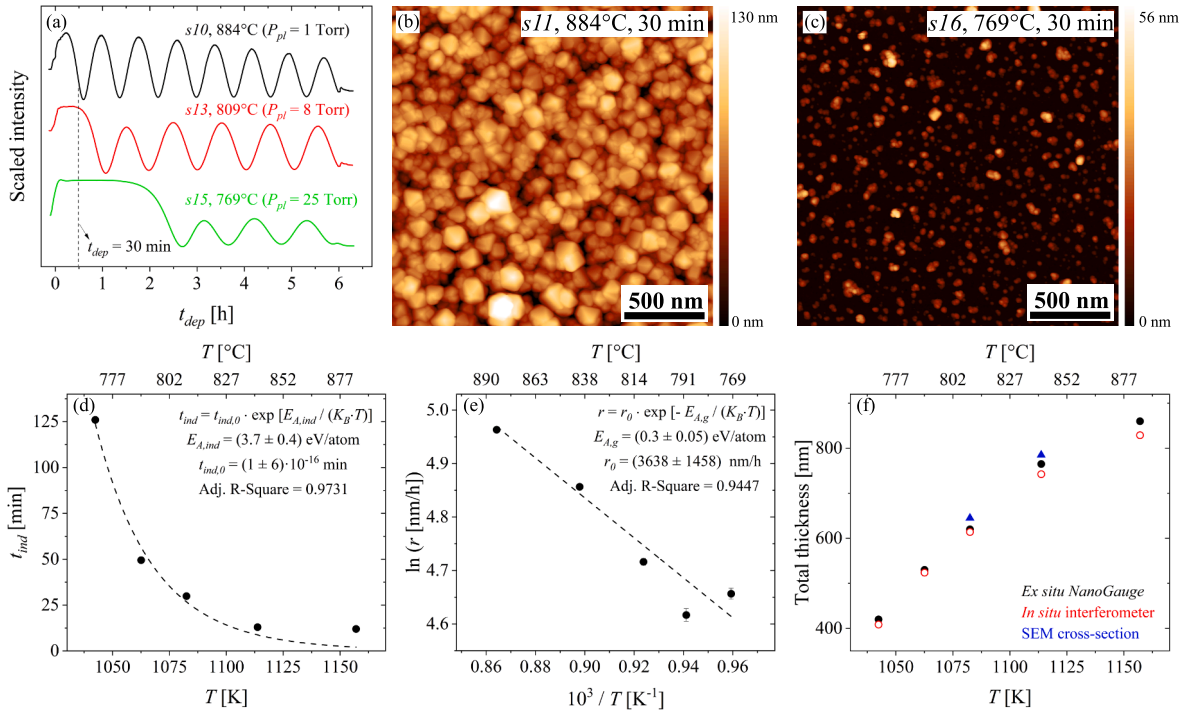

Fig. 4. MWCVD process at P_{ch} = 30 Torr from a gas feed of 1 vol% CH_4 and 0.5 vol% O_2 in H_2 (Table 2). (a) *In situ* interferometer spectra of three selected specimens, namely, (black curve) *s10* (P_{pl} = 1 Torr → T = 884 °C), (red curve) *s13* (P_{pl} = 8 Torr → T = 809 °C), (green curve) *s15* (P_{pl} = 25 Torr → T = 769 °C). The delay of the onset of thickness oscillations was found to be proportional to the growth temperature. In particular, the vertical dashed line shows that, 30 min into the deposition, the interferometer signal was already approaching the first local minimum in sample *s10*, whereas it was still in the induction plateau in sample *s15*. 2 μm × 2 μm AFM image of the surface of (b) sample *s11* and (c) sample *s16*, which were grown for 30 min at T = 884 °C and T = 769 °C, respectively. In line with the interferometer data in (a), (b) and (c) display a compact diamond film and non-coalesced nanodiamonds, respectively. The color bar on the right side of the AFM images represents the height scale. The rms roughness R_q was (b) 19 nm and (c) 4 nm. For samples *s10, s12–15*, (d) plot of the induction time t_{ind} as a function of the growth temperature T, (e) Arrhenius plot of the deposition rate r assessed as illustrated in Fig. 1(b) for sample *s1*, and (f) plot of the total film thickness as a function of the growth temperature T. In (d) the trend of t_{ind} with T was fitted with a function of the form $t_{ind} = t_{ind,0} \exp[E_{A,ind}/(K_B T)]$, where $t_{ind,0}$, $E_{A,ind}$, K_B, and T are the induction time for $T \to \infty$, the apparent activation energy of the induction process, the Boltzmann constant and the absolute temperature in Kelvin, respectively. $E_{A,ind}$ turned out to be 3.7 ± 0.4 eV/atom (86 ± 9 kcal/mol). In (e) the natural logarithm of the deposition rate r was plotted versus the reciprocal of the absolute temperature. An Arrhenius relation of the type $r = r_0 \exp[-E_{A,g}/(K_B T)]$ was fitted to the data. r_0 and $E_{A,g}$ are the asymptotic deposition rate, namely, the deposition rate for $T \to \infty$, and the apparent activation energy of the growth process, respectively. $E_{A,g}$ was found to be 0.3 ± 0.05 eV/atom (7 ± 1 kcal/mol). In (f) the total film thickness was measured *ex situ* by means of the *Optical NanoGauge* (black full circles). The thickness was also estimated as $r \cdot (t_{dep} - t_{ind})$, with r and t_{ind} derived from the *in situ* laser interferometry data (red empty circles), and by taking SEM cross-sections from the center of selected specimens (blue full triangles; Supplementary Figures 1(b–c) of the Supplementary Material).

HFCVD growth of diamond on platinum foils scratched with diamond paste. Belton et al. indeed noticed that the addition of oxygen to the CH_4 and H_2 feed in amounts [O]/[C] ≥ 0.75 suppressed nucleation, whereas growth could be obtained for [O]/[C] = 1 once diamond islands had coalesced. They hypothesized that the nucleation sites, which formed on a precursory graphitic layer stabilized by the scratches, became metastable for high oxygen admixtures [102]. Remarkably, such a commonality, that a nucleation site is more prone to etch in an oxygenated plasma with respect to the crystallites of a developed film, is shared between two material systems, diamond on platinum and diamond on silicon, which nucleate in a dissimilar fashion, the former through the formation of a graphitic deposit and the latter via carburization of the surface.

4. Conclusions

Detonation nanodiamonds were spin-coated with a density of 5 · 10^{10} cm^{-2} on the surface of Si(100) substrates to promote the growth of thin diamond films by MWCVD. Methane, oxygen and hydrogen were employed as the gas mixture in relative concentrations of 1:0.5:98.5. The stability of the seeds was studied as a function of the chamber pressure and the sample temperature. For a chamber pressure P_{ch} of 40 Torr, the sample temperature was varied between 827 °C and 935 °C. At the highest growth temperature of 935 °C, 90% of the seeds were etched by the plasma, likely due to the high structural and chemical defectivity of detonation nanodiamonds. A minority of flawless smaller crystallites survived plasma etching, and were subsequently enlarged by embedding carbon from the methane precursor until the induction stage completed with a characteristic time of 23.5 h, which is circa 65 times longer than for a growth carried out under the same conditions but without an oxygen admixture. Such a long induction time is obviously impractical for any application. Lowering the growth temperature within the accessible interval from 935 °C to 827 °C did not represent a pathway to a more rapid inception of growth, but caused the full dissolution of the seeds. Decreasing P_{ch} from 40 to 30 Torr instead led to a reasonably quick growth induction in spite of the 0.5 vol% oxygen admixture, probably due to a milder attack of the seeds and an increased concentration of nucleation-inducing species at the lower pressure. At P_{ch} = 30 Torr, as the sample temperature was increased across the allowed range from 769 °C to 884 °C, the induction time decayed exponentially from 126 min to 12 min and the film growth rate increased from approximately 100 nm/h to 140 nm/h. The induction time and the film growth rate were observed to depend on the temperature consistent with an Arrhenius law, suggesting that the rate-limiting factors in the induction and the growth process were temperature-dependent surface reactions with apparent activation energies of 3.7 ± 0.4 eV/atom (86 ± 9 kcal/mol) and 0.3 ± 0.05 eV/atom (7 ± 1 kcal/mol), respectively. To the best of our knowledge, this is the first focused investigation of the stability of detonation nanodiamond seeds and the initial stages of the MWCVD of diamond films on silicon substrates in a plasma of methane and hydrogen containing an oxygen admixture. Noteworthily, when at P_{ch} = 30 Torr the oxygen

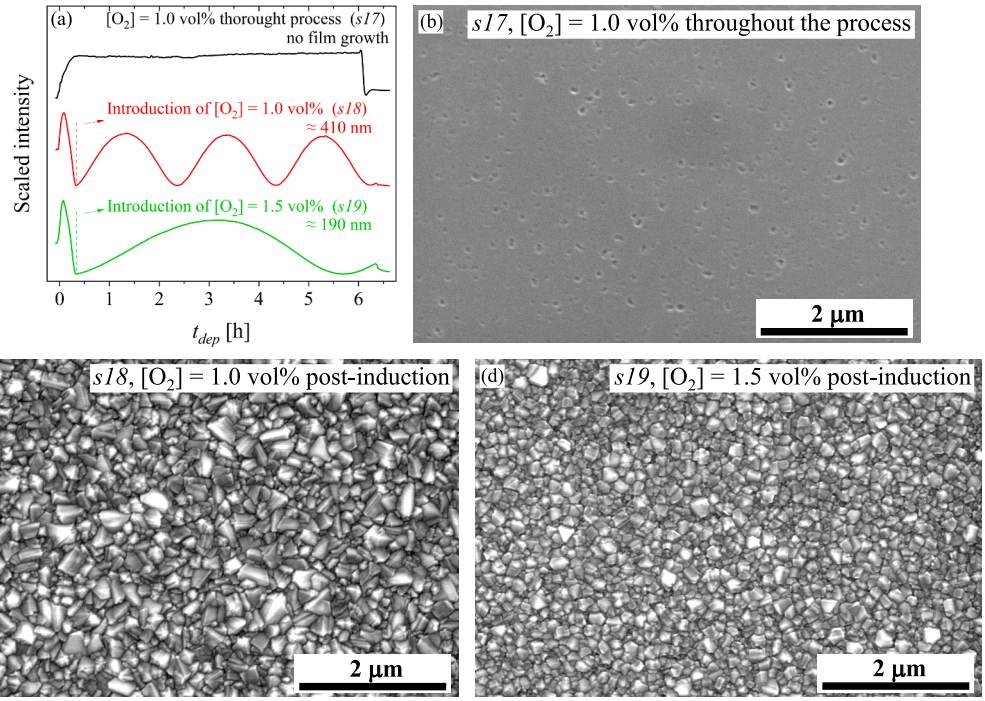

Fig. 5. Samples deposited from a feed of 1 vol% [CH_4] and variable [O_2] in H_2 at P_{ch} = 30 Torr (Table 2). (a) Interferometer curves of (black) *s17* ([O_2] = 1 vol% for 6 h), (red) *s18* ([O_2] = 0 vol% until the first minimum of the interferometer curve, corresponding to approximately 55 nm of thickness (precursor layer), and afterwards [O_2] = 1 vol% for 6 h) and (green) *s19* ([O_2] = 0 vol% until the first minimum of the interferometer curve (precursor layer) and afterwards [O_2] = 1.5 vol% for 6 h). The interferometer data anticipated *in situ* that no growth (no thickness fringes) took place in sample *s17*, whereas film growth occurred with a deposition rate of 56 nm/h and 21 nm/h in sample *s18* and sample *s19*, respectively. The total film thickness, measured *ex situ* with the *Optical Nano Gauge*, was 410 nm and 190 nm for sample *s18* and sample *s19*, respectively. 30000× magnified SEM images of the final surface of (b) *s17*, (c) *s18* and (d) *s19*, revealing (b) etching of the seeds and pitting of the substrate and (c–d) growth of a compact diamond film. SEM imaging of samples *s18-19* was affected by electrical charging owing to the insulating nature of diamond.

concentration in the gas feed was raised from 0.5 to 1 vol%, the seeds were fully etched by the plasma and diamond growth could not be initiated. However, film growth could be successfully carried out under those conditions and even for an oxygen admixture [O_2] = 1.5 vol% on a diamond precursor layer of approximately 55 nm thickness, which was grown in an oxygen-free plasma on a seeded Si(001) substrate. These findings reveal that, within the space of parameters explored, the stability of the seeds primarily depends on the interplay between the chamber pressure and the concentration of the oxygen admixture, and that plasma settings that are unsuitable to initiate seed growth on a chemically dissimilar surface such as silicon can be employed to grow diamond on a pre-existing diamond film.

CRediT authorship contribution statement

Alessandro Giussani: Conceptualization, Investigation, Validation, Formal analysis, Visualization, Writing – original draft, Writing – review & editing. **Stoffel D. Janssens:** Conceptualization, Formal analysis, Visualization, Writing – review & editing. **David Vázquez-Cortés:** Conceptualization, Investigation, Formal analysis, Writing – review & editing. **Eliot Fried:** Funding acquisition, Supervision, Writing – review & editing.

Declaration of competing interest

The authors declare that they have no known competing financial interests or personal relationships that could have appeared to influence the work reported in this paper.

Acknowledgments

The authors gratefully acknowledge the *Okinawa Institute of Science and Technology (OIST) Graduate University* with subsidy funding from the *Cabinet Office, Government of Japan*; Kenjii Ando and Dr. Kazuo Tsugawa from *Seki Diamond Systems*, a division of *CORNES Technologies Ltd.*, for technical advice on the use of the MWCVD reactor; Dr. Igor Kudryashov from *Tokyo Instruments, Inc.* and Dr. Kieran Deasy from *OIST's NanoFab Team* for technical insights on Raman spectroscopy; Dr. Hitoshi Morioka from *Bruker Japan K.K.* and Dr. David C. Lloyd from *OIST* for interesting discussions on X-ray diffraction; Pei Chen King, *Editorial Services, OIST Communication and Public Relations Division*, for proofreading the manuscript.

Appendix A. Supplementary data

Supplementary material related to this article can be found online at https://doi.org/10.1016/j.apsusc.2021.152103.

References

[1] J. Hu, Y.K. Chou, R.G. Thompson, J. Burgess, S. Street, Characterizations of nano-crystalline diamond coating cutting tools, Surf. Coat. Technol. 202 (2007) 1113–1117, http://dx.doi.org/10.1016/j.surfcoat.2007.07.050.

[2] J. Zhang, X. Wang, B. Shen, F. Sun, Effect of boron and silicon doping on improving the cutting performance of CVD diamond coated cutting tools in machining CFRP, Int. J. Refract. Met. Hard Mater. 41 (2013) 285–292, http://dx.doi.org/10.1016/j.ijrmhm.2013.04.017.

[3] J. Zhang, Y. Yuan, J. Zhang, Cutting performance of microcrystalline, nanocrystalline and dual-layer composite diamond coated tools in drilling carbon fiber reinforced plastics, Appl. Sci. 8 (2018) 1642, 1–10, http://dx.doi.org/10.3390/app8091642.

[4] K. Ramasubramanian, N. Arunachalam, M.R. Rao, Performance analysis of nano engineered diamond coated tools for machining of AA2124/SiC_p composite material, Proc. Manuf. 26 (2018) 424–433, http://dx.doi.org/10.1016/j.promfg.2018.07.050.

[5] C.S. Abreu, M. Amaral, F.J. Oliveira, J.R. Gomes, R.F. Silva, HFCVD nanocrystalline diamond coatings for tribo-applications in the presence of water, Diam. Relat. Mater. 18 (2009) 271–275, http://dx.doi.org/10.1016/j.diamond.2008.08.016.

[6] D.W. Wheeler, Applications of diamond to improve tribological performance in the oil and gas industry, Lubricants 6 (2018) 84, 1–27, http://dx.doi.org/10.3390/lubricants6030084.

[7] D. Pradhan, I.N. Lin, Grain-size-dependent diamond-nondiamond composite films: Characterization and field-emission properties, ACS Appl. Mater. Inter. 1 (2009) 1444–1450, http://dx.doi.org/10.1021/am9001327.

[8] B. Huang, S. Jou, M. wu, Field emission and electric discharge of nanocrystalline diamond films, J. Electron. Mater. 38 (2009) 750–755, http://dx.doi.org/10.1007/s11664-009-0706-6.

[9] R.L. Harniman, O.J.L. Fox, W. Janssen, S. Drijkoningen, K. Haenen, P.W. May, Direct observation of electron emission from grain boundaries in CVD diamond by PeakForce-controlled tunnelling atomic force microscopy, Carbon 94 (2015) 386–395, http://dx.doi.org/10.1016/j.carbon.2015.06.082.

[10] M. Wang, P.K. Chu, Nanocrystalline diamond coatings, in: J.L. Shohet (Ed.), Encyclopedia of Plasma Technology, Taylor & Francis Group, Boca Raton, 2016, pp. 857–873, URL http://www.cityu.edu.hk/phy/appkchu/Publications/2016/16.113.pdf.

[11] S.K. Kolekar, R.V. Godbole, V.P. Godbole, C.V. Dharmadhikari, Electron transport across nanocrystalline diamond films: Field emission and conducting atomic force microscopic investigations, AIP Adv. 10 (2020) 045129, http://dx.doi.org/10.1063/1.5142565.

[12] N. Dwivedi, C. Dhand, J.D. Carey, E.C. Anderson, R. Kumar, A.K. Srivastava, H.K. Malik, M.S.M. Saifullah, S. Kumar, R. Lakshminarayanan, S. Ramakrishna, C.S. Bhatia, A. Danner, The rise of carbon materials for field emission, J. Mater. Chem. C 9 (2021) 2620–2659, http://dx.doi.org/10.1039/D0TC05873D.

[13] T.H. Stuchliková, Z. Remes, V. Mortet, A. Taylor, P. Ashcheulov, J. Stuchlik, V.A. Volodin, Electrical and optical characteristics of boron doped nanocrystalline diamond films, Vacuum 168 (2019) 108813, http://dx.doi.org/10.1016/j.vacuum.2019.108813.

[14] E. Petkov, T. Rendler, C. Petkov, F. Schnabel, J.P. Reithmaier, J. Wrachtrup, C. Popov, W. Kulisch, Investigation of NV centers in nano- and ultrananocrystalline diamond pillars, Phys. Status Solidi a 210 (2013) 2066–2073, http://dx.doi.org/10.1002/pssa.201329282.

[15] N. Felgen, B. Naydenov, S. Turner, F. Jelezko, J.P. Reithmaier, C. Popov, Incorporation and study of SiV centers in diamond nanopillars, Diam. Relat. Mater. 64 (2016) 64–69, http://dx.doi.org/10.1016/j.diamond.2016.01.011.

[16] A. Schmidt, B. Naydenov, F. Jelezko, J.P. Reithmaier, C. Popov, Fabrication of highly dense arrays of nanocrystalline diamond nanopillars with integrated silicon-vacancy color centers during the growth, Opt. Mater. Express 9 (2019) 4545–4555, http://dx.doi.org/10.1364/OME.9.004545.

[17] H. Sein, C. Maryan, A. Jones, J. Verran, N. Ali, I.-U. Hassan, C. Rego, W. Ahmed, M.J. Jackson, Diamond surgical tools, in: W. Ahmed, M.J. Jackson (Eds.), Surgical Tools and Medical Devices, Springer International Publishing, Cham, 2016, pp. 149–194, http://dx.doi.org/10.1007/978-3-319-33489-9_7.

[18] W. Ahmed, H. Sein, M. Jackson, C. Rego, I.-U. Hassan, K. Subramani, Chapter 13 - surface engineering of dental tools with diamond for enhanced life and performance, in: K. Subramani, W. Ahmed (Eds.), Emerging Nanotechnologies in Dentistry (Second Edition), in: Micro and Nano Technologies, William Andrew Publishing, 2018, pp. 251–288, http://dx.doi.org/10.1016/B978-0-12-812291-4.00013-3.

[19] C.P. Pennisi, M. Alcaide, Nanocrystalline diamond films for biomedical application, in: S.C..H. Zhu (Ed.), Frontiers in Biomaterials, Vol. 1, Bentham Science Publishers, 2014, pp. 70–100, http://dx.doi.org/10.2174/9781608058761114010006.

[20] A.C. Taylor, B. Vagaska, R. Edgington, C. Hébert, P. Ferretti, P. Bergonzo, R.B. Jackman, Biocompatibility of nanostructured boron doped diamond for the attachment and proliferation of human neural stem cells, J. Neural Eng. 12 (2015) 066016, http://dx.doi.org/10.1088/1741-2560/12/6/066016.

[21] L. Bacakova, A. Broz, J. Liskova, L. Stankova, S. Potocky, A. Kromka, The application of nanodiamond in Biotechnology and tissue engineering, in: M. Aliofkhazraei (Ed.), Diamond and Carbon Composites and Nanocomposites, Intech, 2016, pp. 59–88, http://dx.doi.org/10.5772/63549.

[22] C. Hébert, M. Cottance, J. Degardin, E. Scorsone, L. Rousseau, G. Lissorgues, P. Bergonzo, S. Picaud, Monitoring the evolution of boron doped porous diamond electrode on flexible retinal implant by OCT and in vivo impedance spectroscopy, Mater. Sci. Eng. C Mater. Biol. Appl. 69 (2016) 77–84, http://dx.doi.org/10.1016/j.msec.2016.06.032.

[23] L. Sekaric, J.M. Parpia, H.G. Craighead, T. Feygelson, B.H. Houston, J.E. Butler, Nanomechanical resonant structures in nanocrystalline diamond, Appl. Phys. Lett. 81 (2002) 4455–4457, http://dx.doi.org/10.1063/1.1526941.

[24] A.V. Sumant, O. Auciello, R.W. Carpick, S. Srinivasan, J.E. Butler, Ultrananocrystalline and nanocrystalline diamond thin films for MEMS/NEMS applications, MRS Bull. 35 (2010) 281–288, http://dx.doi.org/10.1557/mrs2010.550.

[25] S.D. Janssens, S. Drijkoningen, K. Haenen, Large piezoresistive effect in surface conductive nanocrystalline diamond, Appl. Phys. Lett. 105 (2014) 101601, http://dx.doi.org/10.1063/1.4895458.

[26] J.E. Butler, A.V. Sumant, The CVD of nanodiamond materials, Chem. Vapor Depos. 14 (2008) 145–160, http://dx.doi.org/10.1002/cvde.200700037.

[27] S.D. Janssens, P. Pobedinskas, J. Vacik, V. Petráková, B. Ruttens, J. D'Haen, M. Nesládek, K. Haenen, P. Wagner, Separation of intra- and intergranular magnetotransport properties in nanocrystalline diamond films on the metallic side of the metal–insulator transition, New J. Phys. 13 (2011) 083008, http://dx.doi.org/10.1088/1367-2630/13/8/083008.

[28] J.J. Gracio, Q.H. Fan, J.C. Madaleno, Diamond growth by chemical vapour deposition, J. Phys. D: Appl. Phys. 43 (2010) 374017, http://dx.doi.org/10.1088/0022-3727/43/37/374017.

[29] O.A. Williams, Nanocrystalline diamond, Diam. Relat. Mater. 20 (2011) 621–640, http://dx.doi.org/10.1016/j.diamond.2011.02.015.

[30] D. Das, Nanocrystalline diamond: A high-impact carbon nanomaterial for multifunctional applications including as nanofiller in biopolymeric matrices, in: S. Yaragalla, R. Mishra, S. Thomas, N. Kalarikkal, H.J. Maria (Eds.), Carbon-Based Nanofillers and their Rubber Nanocomposites, Elsevier, 2019, pp. 123–181, http://dx.doi.org/10.1016/B978-0-12-813248-7.00005-5.

[31] S. Mandal, Nucleation of diamond films on heterogeneous substrates: a review, RSC Adv. 11 (2021) 10159–10182, http://dx.doi.org/10.1039/D1RA00397F.

[32] J. Philip, P. Hess, T. Feygelson, J.E. Butler, S. Chattopadhyay, K.H. Chen, L.C. Chen, Elastic, mechanical, and thermal properties of nanocrystalline diamond films, J. Appl. Phys. 93 (2003) 2164–2171, http://dx.doi.org/10.1063/1.1537465.

[33] F. Silva, F. Bénédic, P. Bruno, A. Gicquel, Formation of <110> texture during nanocrystalline diamond growth: an X-ray diffraction study, Diam. Relat. Mater. 14 (2005) 398–403, http://dx.doi.org/10.1016/j.diamond.2004.11.019.

[34] C.J. Tang, A.J. Neves, S. Pereira, A.J.S. Fernandes, J. Grácio, M.C. Carmo, Effect of nitrogen and oxygen addition on morphology and texture of diamond films (from polycrystalline to nanocrystalline), Diam. Relat. Mater. 17 (2008) 72–78, http://dx.doi.org/10.1016/j.diamond.2007.10.022.

[35] P. Hess, The mechanical properties of various chemical vapor deposition diamond structures compared to the ideal single crystal, J. Appl. Phys. 111 (2012) 051101, http://dx.doi.org/10.1063/1.3683544.

[36] O.A. Williams, A. Kriele, J. Hees, M. Wolfer, W. Müller-Sebert, C.E. Nebel, High Young's modulus in ultra thin nanocrystalline diamond, Chem. Phys. Lett. 495 (2010) 84–89, http://dx.doi.org/10.1016/j.cplett.2010.06.054.

[37] O. Auciello, D. Aslam, Review on advances in microcrystalline, nanocrystalline and ultrananocrystalline diamond films-based micro/nano-electromechanical systems technologies, J. Mater. Sci. 56 (2021) 7171–7230, http://dx.doi.org/10.1007/s10853-020-05699-9.

[38] T. Kawato, K.-I. Kondo, Effects of oxygen on CVD diamond synthesis, Japan. J. Appl. Phys. 26 (1987) 1429–1432, http://dx.doi.org/10.1143/jjap.26.1429.

[39] J.A. Mucha, D.L. Flamm, D.E. Ibbotson, On the role of oxygen and hydrogen in diamond-forming discharges, J. Appl. Phys. 65 (1989) 3448–3452, http://dx.doi.org/10.1063/1.342635.

[40] Y. Liou, A. Inspektor, R. Weimer, D. Knight, R. Messier, The effect of oxygen in diamond deposition by microwave plasma enhanced chemical vapor deposition, J. Mater. Res. 5 (1990) 2305–2312, http://dx.doi.org/10.1557/JMR.1990.2305.

[41] Y. Muranaka, H. Yamashita, H. Miyadera, Characterization of diamond films synthesized in the microwave plasmas of CO/H_2 and $CO/O_2/H_2$ systems at low temperatures (403–1023 K), J. Appl. Phys. 69 (1991) 8145–8153, http://dx.doi.org/10.1063/1.347468.

[42] C.J. Tang, L.P. Gu, J. Grácio, J.L. Ribeiro, Role of oxygen additive on hydrogen impurity incorporation in nanocrystalline diamond films fabricated by microwave plasma chemical vapor deposition, Phys. Status Solidi a 206 (2009) 2816–2821, http://dx.doi.org/10.1002/pssa.200925147.

[43] J. Ruan, K. Kobashi, W.J. Choyke, Effect of oxygen on boron doping in chemical vapor deposition of diamond as deduced from cathodoluminescence studies, Appl. Phys. Lett. 60 (1992) 1884–1886, http://dx.doi.org/10.1063/1.107143.

[44] R. Erz, W. Dötter, K. Jung, H. Ehrhardt, Investigation of boron and hydrogen concentrations in p-type diamond films by infrared spectroscopy, Diam. Relat. Mater. 4 (1995) 469–472, http://dx.doi.org/10.1016/0925-9635(94)05320-0.

[45] I. Sakaguchi, M. Nishitani-Gamo, K. Loh, K. Yamamoto, H. Haneda, T. Ando, Effect of oxygen addition on boron incorporation on semiconductive diamond CVD, Diam. Relat. Mater. 7 (1998) 1144–1147, http://dx.doi.org/10.1016/S0925-9635(98)00161-7.

[46] P. Bou, L. Vandenbulcke, R. Herbin, F. Hillion, Diamond film nucleation and interface characterization, J. Mater. Res. 7 (1992) 2151–2159, http://dx.doi.org/10.1557/JMR.1992.2151.

[47] I. Sakaguchi, M. Nishitani-Gamo, K.P. Loh, H. Haneda, S. Hishita, T. Ando, Silicon incorporation into chemical vapor deposition diamond: A role of oxygen, Appl. Phys. Lett. 71 (1997) 629–631, http://dx.doi.org/10.1063/1.119812.

[48] X. Zhang, Y. Cui, X. Liu, T. Sui, C. Ji, D. Zhang, Wettability modulation of nano-crystalline diamond films via in-situ CVD process, Surf. Coat. Technol. 375 (2019) 681–687, http://dx.doi.org/10.1016/j.surfcoat.2019.07.069.

[49] T. Izak, O. Babchenko, M. Varga, S. Potocky, A. Kromka, Low temperature diamond growth by linear antenna plasma CVD over large area, Phys. Status Solidi b 249 (2012) 2600–2603, http://dx.doi.org/10.1002/pssb.201200103.

[50] J. Zalieckas, P. Pobedinskas, M.M. Greve, K. Eikehaug, K. Haenen, B. Holst, Large area microwave plasma CVD of diamond using composite right/left-handed materials, Diam. Relat. Mater. 116 (2021) 108394, http://dx.doi.org/10.1016/j.diamond.2021.108394.

[51] S. Drijkoningen, P. Pobedinskas, S. Korneychuk, A. Momot, Y. Balasubramaniam, M.K. Van Bael, S. Turner, J. Verbeeck, M. Nesládek, K. Haenen, On the origin of diamond plates deposited at low temperature, Cryst. Growth Des. 17 (2017) 4306–4314, http://dx.doi.org/10.1021/acs.cgd.7b00623.

[52] G.W. Gale, R.J. Small, K.A. Reinhardt, Aqueous cleaning and surface conditioning processes, in: K.A. Reinhardt, W. Kern (Eds.), Handbook of Silicon Wafer Cleaning Technology (Second Edition), William Andrew Publishing, Norwich, NY, 2008, pp. 201–265, http://dx.doi.org/10.1016/B978-081551554-8.50007-0.

[53] S.D. Janssens, D. Vázquez-Cortés, A. Giussani, J.A. Kwiecinski, E. Fried, Nanocrystalline diamond-glass platform for the development of three-dimensional micro- and nanodevices, Diam. Relat. Mater. 98 (2019) 107511, http://dx.doi.org/10.1016/j.diamond.2019.107511.

[54] P. Pobedinskas, G. Degutis, W. Dexters, J. D'Haen, M. Van Bael, K. Haenen, Nanodiamond seeding on plasma-treated tantalum thin films and the role of surface contamination, Appl. Surf. Sci. 538 (2021) 148016, http://dx.doi.org/10.1016/j.apsusc.2020.148016.

[55] S.D. Janssens, B. Sutisna, A. Giussani, J.A. Kwiecinski, D. Vázquez-Cortés, E. Fried, Boundary curvature effect on the wrinkling of thin suspended films, Appl. Phys. Lett. 116 (2020) 193702, http://dx.doi.org/10.1063/5.0006164.

[56] O.A. Williams, M. Nesladek, M. Daenen, S. Michaelson, A. Hoffman, E. Osawa, K. Haenen, R.B. Jackman, Growth, electronic properties and applications of nanodiamond, Diam. Relat. Mater. 17 (2008) 1080–1088, http://dx.doi.org/10.1016/j.diamond.2008.01.103.

[57] S.-L. Zhang, R. Buchta, D. Sigurd, Rapid thermal processing with microwave heating, Thin Solid Films 246 (1994) 151–157, http://dx.doi.org/10.1016/0040-6090(94)90744-7.

[58] O.A. Williams, M. Daenen, J. D'Haen, K. Haenen, J. Maes, V.V. Moshchalkov, M. Nesládek, D.M. Gruen, Comparison of the growth and properties of ultra-nanocrystalline diamond and nanocrystalline diamond, Diam. Relat. Mater. 15 (2006) 654–658, http://dx.doi.org/10.1016/j.diamond.2005.12.009.

[59] S. Saada, S. Pochet, L. Rocha, J. Arnault, P. Bergonzo, Real time investigation of diamond nucleation by laser scattering, Diam. Relat. Mater. 18 (2009) 707–712, http://dx.doi.org/10.1016/j.diamond.2009.01.044.

[60] T. Satō, Spectral emissivity of silicon, Japan. J. Appl. Phys. 6 (1967) 339–347, http://dx.doi.org/10.1143/jjap.6.339.

[61] N.M. Ravindra, B. Sopori, O.H. Gokce, S.X. Cheng, A. Shenoy, L. Jin, S. Abedrabbo, W. Chen, Y. Zhang, Emissivity measurements and modeling of silicon-related materials: An overview, Int. J. Thermophys. 22 (2001) 1593–1611, http://dx.doi.org/10.1023/A:1012869710173.

[62] A.J. SpringThorpe, T.P. Humphreys, A. Majeed, W.T. Moore, In situ growth rate measurements during molecular beam epitaxy using an optical pyrometer, Appl. Phys. Lett. 55 (1989) 2138–2140, http://dx.doi.org/10.1063/1.102082.

[63] B.R. Stoner, B.E. Williams, S.D. Wolter, K. Nishimura, J.T. Glass, In situ growth rate measurement and nucleation enhancement for microwave plasma CVD of diamond, J. Mater. Res. 7 (1992) 257–260, http://dx.doi.org/10.1557/JMR.1992.0257.

[64] H. Liu, D.S. Dandy, Studies on nucleation process in diamond CVD: an overview of recent developments, Diam. Relat. Mater. 4 (1995) 1173–1188, http://dx.doi.org/10.1016/0925-9635(96)00297-2.

[65] R. Meilunas, M.S. Wong, K.C. Sheng, R.P.H. Chang, R.P. Van Duyne, Early stages of plasma synthesis of diamond films, Appl. Phys. Lett. 54 (1989) 2204–2206, http://dx.doi.org/10.1063/1.101124.

[66] B.E. Williams, J.T. Glass, Characterization of diamond thin films: Diamond phase identification, surface morphology, and defect structures, J. Mater. Res. 4 (1989) 373–384, http://dx.doi.org/10.1557/JMR.1989.0373.

[67] D.N. Belton, S.J. Harris, S.J. Schmieg, A.M. Weiner, T.A. Perry, In situ characterization of diamond nucleation and growth, Appl. Phys. Lett. 54 (1989) 416–417, http://dx.doi.org/10.1063/1.100938.

[68] F.G. Celii, J.E. Butler, Diamond chemical vapor deposition, Annu. Rev. Phys. Chem. 42 (1991) 643–684, http://dx.doi.org/10.1146/annurev.pc.42.100191.003235.

[69] S.I. Shah, M.M. Waite, Effect of oxygen on the nucleation and growth of diamond thin films, Appl. Phys. Lett. 61 (1992) 3113–3115, http://dx.doi.org/10.1063/1.107977.

[70] M.M. Waite, S.I. Shah, X-ray photoelectron spectroscopy of initial stages of nucleation and growth of diamond thin films during plasma assisted chemical vapor deposition, Appl. Phys. Lett. 60 (1992) 2344–2346, http://dx.doi.org/10.1063/1.107474.

[71] B.R. Stoner, G.-H.M. Ma, S.D. Wolter, J.T. Glass, Characterization of bias-enhanced nucleation of diamond on silicon by invacuo surface analysis and transmission electron microscopy, Phys. Rev. B 45 (1992) 11067–11084, http://dx.doi.org/10.1103/PhysRevB.45.11067.

[72] F. Arezzo, N. Zacchetti, W. Zhu, X-ray photoelectron spectroscopy study of substrate surface pretreatments for diamond nucleation, J. Appl. Phys. 75 (1994) 5375–5381, http://dx.doi.org/10.1063/1.355692.

[73] X. Jiang, K. Schiffmann, C.-P. Klages, Nucleation and initial growth phase of diamond thin films on (100) silicon, Phys. Rev. B 50 (1994) 8402–8410, http://dx.doi.org/10.1103/PhysRevB.50.8402.

[74] X. Jiang, C.-P. Klages, Recent developments in heteroepitaxial nucleation and growth of diamond on silicon, Phys. Status Solidi a 154 (1996) 175–183, http://dx.doi.org/10.1002/pssa.2211540114.

[75] J.C. Arnault, S. Hubert, F. Le Normand, Silicon etching during the HFCVD diamond growth, J. Phys. Chem. B 102 (1998) 4856–4864, http://dx.doi.org/10.1021/jp9809742.

[76] J.C. Arnault, S. Saada, M. Nesladek, O.A. Williams, K. Haenen, P. Bergonzo, E. Ōsawa, Diamond nanoseeding on silicon: Stability under H_2 MPCVD exposures and early stages of growth, Diam. Relat. Mater. 17 (2008) 1143–1149, http://dx.doi.org/10.1016/j.diamond.2008.01.008.

[77] E. Thomas, S. Mandal, Ashek-I-Ahmed, J.E. Macdonald, T.G. Dane, J. Rawle, C.L. Cheng, O.A. Williams, Spectroscopic ellipsometry of nanocrystalline diamond film growth, ACS Omega 2 (2017) 6715–6727, http://dx.doi.org/10.1021/acsomega.7b00866.

[78] C. Bittencourt, Reaction of Si (100) with silane–methane low-power plasma: SiC buffer-layer formation, J. Appl. Phys. 86 (1999) 4643–4648, http://dx.doi.org/10.1063/1.371415.

[79] D.R. Olander, M. Balooch, J. Abrefah, W.J. Siekhaus, Modulated molecular-beam studies of the surface chemistry of silicon reaction with reactive gases, J. Vac. Sci. Technol. B 5 (1987) 1404–1409, http://dx.doi.org/10.1116/1.583625.

[80] Y. Wei, L. Li, I.S.T. Tsong, Etching of Si(111)-(7x7) and Si(100)-(2x1) surfaces by atomic hydrogen, Appl. Phys. Lett. 66 (1995) 1818–1820, http://dx.doi.org/10.1063/1.113332.

[81] S. Turner, O.I. Lebedev, O. Shenderova, I.I. Vlasov, J. Verbeeck, G. Van Tendeloo, Determination of size, morphology, and nitrogen impurity location in treated detonation nanodiamond by transmission electron microscopy, Adv. Funct. Mater. 19 (2009) 2116–2124, http://dx.doi.org/10.1002/adfm.200801872.

[82] S. Osswald, V.N. Mochalin, M. Havel, G. Yushin, Y. Gogotsi, Phonon confinement effects in the Raman spectrum of nanodiamond, Phys. Rev. B 80 (2009) 075419, http://dx.doi.org/10.1103/PhysRevB.80.075419.

[83] A.V. Kvit, V.V. Zhirnov, T. Tyler, J.J. Hren, Aging effect and nitrogen distribution in diamond nanoparticles, Composites B 35 (2004) 163–166, http://dx.doi.org/10.1016/j.compositesb.2003.08.003.

[84] A. Krüger, F. Kataoka, M. Ozawa, T. Fujino, Y. Suzuki, A. Aleksenskii, A.Y. Vul', E. Ōsawa, Unusually tight aggregation in detonation nanodiamond: Identification and disintegration, Carbon 43 (8) (2005) 1722–1730, http://dx.doi.org/10.1016/j.carbon.2005.02.020.

[85] O.O. Mykhaylyk, Y.M. Solonin, D.N. Batchelder, R. Brydson, Transformation of nanodiamond into carbon onions: A comparative study by high-resolution transmission electron microscopy, electron energy-loss spectroscopy, x-ray diffraction, small-angle x-ray scattering, and ultraviolet Raman spectroscopy, J. Appl. Phys. 97 (2005) 074302, http://dx.doi.org/10.1063/1.1868054.

[86] M. Yeganeh, P.R. Coxon, A.C. Brieva, V.R. Dhanak, L. Šiller, Y.V. Butenko, Atomic hydrogen treatment of nanodiamond powder studied with photoemission spectroscopy, Phys. Rev. B 75 (2007) 155404, http://dx.doi.org/10.1103/PhysRevB.75.155404.

[87] C. Bradac, T. Gaebel, N. Naidoo, J.R. Rabeau, A.S. Barnard, Prediction and measurement of the size-dependent stability of fluorescence in diamond over the entire nanoscale, Nano Lett. 9 (2009) 3555–3564, http://dx.doi.org/10.1021/nl9017379.

[88] V. Pichot, O. Stephan, M. Comet, E. Fousson, J. Mory, K. March, D. Spitzer, High nitrogen doping of detonation nanodiamonds, J. Phys. Chem. C 114 (2010) 10082–10087, http://dx.doi.org/10.1021/jp9121485.

[89] K. Reichelt, Nucleation and growth of thin films, Vacuum 38 (1988) 1083–1099, http://dx.doi.org/10.1016/0042-207X(88)90004-8.

[90] X. Jiang, K. Schiffmann, A. Westphal, C.-P. Klages, Atomic-force-microscopic study of heteroepitaxial diamond nucleation on (100) silicon, Appl. Phys. Lett. 63 (1993) 1203–1205, http://dx.doi.org/10.1063/1.109771.

[91] H. Buchkremer-Hermanns, H. Ren, G. Kohlschein, H. Weiß, Nucleation and early growth of CVD diamond on silicon nitride, Surf. Coat. Technol. 98 (1998) 1038–1046, http://dx.doi.org/10.1016/S0257-8972(97)00237-5.

[92] Y. Hayashi, W. Drawl, R. Messier, Temperature dependence of nucleation density of chemical vapor deposition diamond, Jpn. J. Appl. Phys. 31 (1992) L193–L196, http://dx.doi.org/10.1143/jjap.31.l193.

[93] X. Ning, Z. Zhihao, S. Zhuo, Z. Xiaofeng, X. Chunfang, W. Peiming, X. Peisheng, Selected-area diamond deposition on Si substrates pre-treated in different ways, Surf. Coat. Technol. 63 (1994) 159–165, http://dx.doi.org/10.1016/0257-8972(94)90093-0.

[94] H. Buchkremer-Hermanns, H. Ren, J. Utsch, H. Weiss, Optimization of MW-PACVD diamond deposition parameters for high nucleation density and growth rate on Si_3N_4 substrate, Diam. Relat. Mater. 6 (1997) 411–416, http://dx.doi.org/10.1016/S0925-9635(96)00711-X.

[95] D.G. Kim, H.C. Lee, J.Y. Lee, Effect of reaction pressure on the nucleation behaviour of diamond synthesized by hot-filament chemical vapour deposition, J. Mater. Sci. 28 (1993) 6704–6708, http://dx.doi.org/10.1007/BF00356418.

[96] S.T. Lee, Y.W. Lam, Z. Lin, Y. Chen, Q. Chen, Pressure effect on diamond nucleation in a hot-filament CVD system, Phys. Rev. B 55 (1997) 15937–15941, http://dx.doi.org/10.1103/PhysRevB.55.15937.

[97] W. Zhu, R. Messier, A.R. Badzian, Effects of process parameters on CVD diamond films, in: First International Symposium on Diamond and Diamond-Like Films, in: ECS Proceedings Volumes, Vol. 89–12, The Electrochemical Society, Pennington, NJ, 1989, pp. 61–79.

[98] T.G. McCauley, D.M. Gruen, A.R. Krauss, Temperature dependence of the growth rate for nanocrystalline diamond films deposited from an Ar/CH_4 microwave plasma, Appl. Phys. Lett. 73 (1998) 1646–1648, http://dx.doi.org/10.1063/1.122233.

[99] S. Potocky, A. Kromka, J. Potmesil, Z. Remes, Z. Polackova, M. Vanecek, Growth of nanocrystalline diamond films deposited by microwave plasma CVD system at low substrate temperatures, Phys. Status Solidi a 203 (2006) 3011–3015, http://dx.doi.org/10.1002/pssa.200671110.

[100] S.Z. Rotter, J.C. Madaleno, Diamond CVD by a combined plasma pretreatment and seeding procedure, Chem. Vap. Depos. 15 (2009) 209–216, http://dx.doi.org/10.1002/cvde.200806745.

[101] E. Kondoh, T. Ohta, T. Mitomo, K. Ohtsuka, Determination of activation energies for diamond growth by an advanced hot filament chemical vapor deposition method, Appl. Phys. Lett. 59 (1991) 488–490, http://dx.doi.org/10.1063/1.105417.

[102] D.N. Belton, S.J. Schmieg, Nucleation of chemically vapor deposited diamond on platinum and nickel substrates, Thin Solid Films 212 (1992) 68–80, http://dx.doi.org/10.1016/0040-6090(92)90502-3.